



LAWRENCE
LIVERMORE
NATIONAL
LABORATORY

Spectroscopy of a New Kind of Cluster-Scale Gravitational Lens

S. M. Ammons, K. C. Wong, C. R. Keeton, A. I.
Zabludoff

January 3, 2013

The Astrophysical Journal

Disclaimer

This document was prepared as an account of work sponsored by an agency of the United States government. Neither the United States government nor Lawrence Livermore National Security, LLC, nor any of their employees makes any warranty, expressed or implied, or assumes any legal liability or responsibility for the accuracy, completeness, or usefulness of any information, apparatus, product, or process disclosed, or represents that its use would not infringe privately owned rights. Reference herein to any specific commercial product, process, or service by trade name, trademark, manufacturer, or otherwise does not necessarily constitute or imply its endorsement, recommendation, or favoring by the United States government or Lawrence Livermore National Security, LLC. The views and opinions of authors expressed herein do not necessarily state or reflect those of the United States government or Lawrence Livermore National Security, LLC, and shall not be used for advertising or product endorsement purposes.

SPECTROSCOPY OF A NEW KIND OF CLUSTER-SCALE GRAVITATIONAL LENS

S. MARK AMMONS¹, KENNETH C. WONG², CHARLES R. KEETON³, ANN I. ZABLUDOFF²

Draft version January 2, 2013

ABSTRACT

Using Luminous Red Galaxies (LRGs) as tracers of multiple cluster-scale mass overdensities along the line-of-sight can identify superior cosmic telescopes with higher integrated masses and complex lens plane interactions that boost the étendue. We present galaxy spectroscopy and preliminary magnification maps for two such lines of sight with integrated virial masses exceeding $\sim 3 \times 10^{15} M_{\odot}$. From 979 MMT Hectospec spectra, we identify 2-3 groups and cluster-scale halos in each beam. The majority of the mass in beam 0850 is contributed by Abell 1682, a single massive cluster at $z = 0.3774$, whereas 1306 is composed of three clusters with virial masses between $7 \times 10^{14} M_{\odot}$ and $1.9 \times 10^{15} M_{\odot}$. We confirm the lensing power of these beams with the discovery of eight strongly lensed arcs, visible in multi-band HST and Subaru Suprime-Cam imaging. We identify in ground-based seeing a serendipitous multiply-imaged V-dropout source at $z = 4.95$ in beam 0850. The location of the multiply-imaged arcs is consistent with the predicted critical curves for a source plane of $z = 4.95$ for a mass model derived from galaxy spectroscopy alone. The significant lensing power of these beams makes them important for future studies of reionization and galaxy formation in the early universe now and in the era of JWST.

Subject headings:

1. INTRODUCTION

Measurement of the properties of high-redshift galaxies is the first step towards identifying the sources of reionizing photons and understanding the initial stages of the formation of galaxies. Progress in this arena is limited by the sensitivity of telescope instrumentation and the intrinsic faintness of high-redshift galaxies. One productive technique for selecting high-redshift galaxies is the dropout method in blank fields (Bouwens et al. 2008, 2010; Bunker et al. 2010). These studies use deep imaging to select sources via the sharp Lyman Break feature, a combination of Lyman alpha emission and the absorption of intergalactic neutral hydrogen, which causes the source to “drop out” of the band on the blue side of the break. Studies based on the dropout selection method at $z \sim 10$ suggest that the decrease in the characteristic luminosity of galaxies (M^*) with redshift seen at $3 < z < 7$ continues to $z \sim 10$ and beyond (Yan et al. 2010; Bouwens et al. 2011, 2012; Oesch et al. 2012; Ellis et al. 2012).

A promising technique for increasing the number of source detections at high redshifts is the “cosmic telescope” method (Zwicky 1937) in which a foreground cluster is used to magnify distant faint objects into detectability. Galaxy clusters can assist in constraining the luminosity function by boosting number counts, especially at the faint end, resulting in detections of sources that would not be detectable otherwise (Richard et al. 2006, 2008; Stark et al. 2007; Bouwens et al. 2009; Bradač et al. 2009; Hall et al. 2012). In addition to increasing number counts in deep surveys, cosmic lensing makes

more photons in individual sources available for spectroscopy, helpful for following-up detections made with photometric methods. However, lensing techniques are also subject to a loss of volume probed (Broadhurst, Taylor, & Peacock 1995a), and so one of the principal advantages of lensing has been assumed to be the ability to constrain the faint end slope (Richard et al. 2008).

Cosmic telescopes can potentially benefit a wide variety of science in extragalactic astronomy and cosmology. Surveys at redshifts beyond 1 that require good depth, but do not suffer from a loss of volume probed (i.e., the objects at the luminosities probed are not extremely rare, e.g., QSOs), can benefit in terms of signal-to-noise and number of detected sources at fainter intrinsic luminosities. Lensing also provides improved spatial resolution, permitting the study of individual objects at resolutions 2-10x better than available with single-aperture telescopes. In general, cosmic telescopes allow one to push 1-2 magnitudes fainter than the long-exposure observational limit of current telescopes, and so will be important for studies of the first stars and galaxies at $z > 10$.

Lensing is currently being used to constrain the $z \gtrsim 7$ luminosity function at fainter intrinsic magnitudes than blank field studies with comparable exposure time. Coe et al. (2013) uses a multiply-imaged $z \sim 11$ candidate in the lensing field of MACSJ0647.7+7015 to place constraints on the star formation rate density at $z \sim 11$. Hall et al. (2012) finds ten $z \sim 7$ candidates using dropout selection in the field of the Bullet Cluster, including two multiply-imaged sources and one spectroscopically confirmed object (Bradač et al. 2012). A number of other high-redshift discoveries have been made in lensing fields (Broadhurst & Lehar 1995b; Ebbels et al. 1996; Franx et al. 1997; Frye & Broadhurst 1998; Kneib et al. 2004; Bradley et al. 2008; Zheng et al. 2009, 2012).

The usefulness of a cosmic telescope in increasing number counts can be understood through its étendue, or

¹ Lawrence Livermore National Laboratory, Physics Division L-210, 7000 East Ave., Livermore CA 94550, ammons1@llnl.gov

² Steward Observatory, University of Arizona, 933 Cherry Ave., Tucson, AZ 85721, kwong@as.arizona.edu, aiz@email.arizona.edu

³ Department of Physics and Astronomy, Rutgers University, 136 Frelinghuysen Road, Piscataway, NJ 08854, keeton@physics.rutgers.edu

areal coverage in the source plane with magnification over a pre-defined threshold. Cosmic telescopes with multiple projected structures along the line of sight can theoretically have larger étendue than available single-cluster lenses for two reasons. First, beams with multiple projected structures can potentially have higher integrated masses and thus larger regions of high magnification. Second, multiple structures create lensing interactions that can boost the étendue of the beam (Wong et al. 2012). In this paper, we present J085007.6+360428 and J130657.5+463219 (hereafter referred to as “0850” and “1306”), the first two lines of sight we have selected from the SDSS using LRGs to trace mass overdensities projected in 3′5-radius beams (Wong et al. 2013). The composition of the beams reflect the diversity seen in the LRG sample, with a single massive cluster dominating 0850 and multiple clusters of $\sim 1 \times 10^{15} M_{\odot}$ populating 1306.

In this paper we present MMT Hectospec spectroscopy that we use to constrain the virial masses and radii of the line of sight structures in each beam. We also present public Subaru Suprime-Cam imaging that displays several strongly lensed arcs visible in ground-based seeing, including a new multiply-imaged source at $z = 4.95$. Although we do not use the arcs to constrain the mass model at this time, we test that the locations of critical curves predicted by the mass model derived from the spectroscopy alone are consistent with the coordinates of the detected arcs. Section 2 summarizes the Wong et al. (2013) technique used to select our parent sample of beams from the SDSS, as well as what is known in the literature about 0850 and 1306. Section 3 presents the MMT Hectospec spectroscopy and Subaru Suprimecam imaging and data reduction for both. Section 4 presents the spatial and kinematic properties of the structures in the redshift maps. Section 4.4 describes the mass models and resulting magnification maps derived from the spectroscopic data using GRAVLENS (Keeton 2001). We discuss possible errors in the magnification maps. Section 4.5 describes the multiply-imaged arcs seen in the Subaru imaging and compares them to the predicted critical curve locations. Section 5 summarizes our conclusions. A Λ CDM cosmology is assumed throughout, with $H_0 = 71 \text{ km s}^{-1} \text{ Mpc}^{-1}$, $\Omega_M = 0.27$, and $\Omega_{\Lambda} = 0.73$. For readability, we omit the h convention with the understanding that masses and radii are in units of h_{71}^{-1} and luminosities are in units of h_{71}^{-2} .

2. BEAM SELECTION AND PROPERTIES

2.1. Selection Technique

Our parent sample of dense beams is selected from the SDSS Data Release 9 (DR9; Ahn et al. 2012). The beams are selected to have large concentrations of LRGs to identify beams with a large total mass and possibly multiple projected structures. The details of the beam selection are presented in Wong et al. (in preparation) and briefly summarized here. We compute the total LRG rest-frame i' -band luminosity in 3′5-radius apertures in the redshift range $0.1 < z < 0.7$. We then sort the list by total LRG luminosity and identify the 200 best beams. LRGs are biased tracers of the underlying mass distribution, so we expect that the fields with the greatest luminosity in LRGs are also the beams with the

greatest total mass. The 3′5 radius is chosen to select beams with a large region of high magnification and to match the typical field size of infrared multi-object spectrographs for follow-up. The result of the selection is a sample of beams with integrated LRG luminosities of $7.2 \times 10^{11} < L_i < 1.3 \times 10^{12} h^{-2} L_{\odot}$.

The two beams presented in this paper were originally selected from an earlier version of our list of beams based on the Padmanabhan et al. (2005) LRG catalog, although they are both within the top 200 beams presented in Wong et al. (2013). For this reason, the beam centers presented here differ from the coordinates given in Wong et al. (2013) by $\sim 15''$ in 0850 and $\sim 107''$ in 1306. Our spectroscopic targeting completeness across these fields ensures that we still cover the most significant mass peaks in both fields.

2.2. Properties of 0850 and 1306

The two beams we present are the first selected from the parent sample of 200 beams for their high integrated LRG luminosities. Both harbor known massive galaxy clusters - Zwicky 1953 for 0850 (Zwicky et al. 1961) and Abell 1682 for 1306 (Abell 1989). There are also two Gaussian Mixture Brightest Cluster Galaxy (GMBCG) associations within 3′5 of the field center of 0850: J132.49437+36.10756 at a photometric redshift of $z = 0.284$ and J132.52774+36.01979 at a photometric redshift of $z = 0.241$ (Hao et al. 2010). There are four additional associations within 3′5 of the field center of 1306, including WHL J130657.3+463206 at a redshift of $z = 0.2081$ (Wen et al. 2009), NSC J130639+463208 with a photometric redshift of $z = 0.2508$ (Gal et al. 2003), GMBCG J196.70832+46.55927 at $z = 0.245$, and GMBCG J196.75262+46.56389 at $z = 0.337$ (Hao et al. 2010). We discuss the overlap between these photometrically-identified groups and the groups we identify with field spectroscopy in Section 4.3.

Extended X-ray sources were seen at these locations with ROSAT, giving X-ray luminosities in the 0.1-2.4 keV band (cluster rest frame) of $1.1 \times 10^{44} \text{ ergs s}^{-1}$ and $3.4 \times 10^{44} \text{ ergs s}^{-1}$ for 1306 and 0850, respectively (Ebeling et al. 1998). 0850 is a member of the ROSAT Brightest Cluster Catalog (Ebeling et al. 1998; Crawford et al. 1999) and the Northern ROSAT All-Sky (NORAS) Galaxy Cluster Survey (Böhringer et al. 2000). The principal cluster was identified optically in the Second Palomar Observatory Sky Survey (Djorgovski et al. 1999) with a photometric redshift of 0.314 (Gal et al. 2003). The X-ray temperature for 0850 is $\langle kT \rangle = 7.37 \text{ keV}$ from Chandra (Cavagnolo et al. 2009) and 14.5 keV from ROSAT (Ebeling et al. 1998).

3. DATA AND REDUCTION

3.1. Galaxy Spectroscopy

We have completed a redshift survey of 959 field galaxies in these two beams with MMT Hectospec, a multi-object optical spectrograph with 300 fibers accessing a 1 degree field of view (Fabricant et al. 2005; Mink et al. 2007). Fiber crowding limits the number of galaxies that can be targeted in the central 7′0 diameter of our fields to $\sim 30 - 40$ per exposure. However, many fibers are available beyond this diameter to sample the outskirts of the centralized structures.

TABLE 1

BEAM PROPERTIES. BEAM LOCATIONS ARE GIVEN AS THE COORDINATES OF THE LRG ON WHICH THE $3\frac{1}{2}$ RADIUS CIRCLE USED TO COUNT LRGs WAS CENTERED.

Beam name	RA (J2000)	Dec (J2000)	L_X (ergs s $^{-1}$)	$L_{LRG}(L_{sun})$	Number of LRGs	Comments
0850	08 50 07.58	+36 04 27.9	3.4×10^{44}	1×10^{12}	15	Zwicky 1953 (08 50 11.2 +36 04 21)
1306	13 06 57.51	+46 32 19.4	1.1×10^{44}	1×10^{12}	14	Abell 1682 (13 06 49.7 +46 32 59)

Hectospec’s grating with 270 grooves mm $^{-1}$ delivers a spectral resolution of $\sim 4.5 - 5.2 \text{ \AA}$ ($R \sim 750 - 1800$) and a spectral coverage of 3650 – 9200 \AA with a central wavelength of 6500 \AA . This wavelength coverage was selected to include [OII] emission features, Ca II H + K absorption, and $H\beta$ emission for galaxies in the range $0 < z < 0.7$. This redshift range samples the structures associated with the LRGs our catalog (Wong et al. 2013).

Specialized “bright” configurations with one hour total exposure time included SDSS targets with $i_{AB} < 20.5$. “Faint” configurations with 2 hour exposure times included SDSS targets with $20.5 < i_{AB} < 21.1$.

Fiber configurations for Hectospec were designed with the CfA *xfitfibs* software. Configurations acquired before June 2011 typically included only targets within a 7 arcminute radius of the beam centers and configurations acquired afterwards included targets out to a 15 arcminute radius. 5 – 10 F stars were included in each fiber configuration to enable flux calibration and removal of atmospheric absorption features. *xfitfibs* also permits inclusion of fibers for lower priority objects such that they do not interfere with high-priority objects; when possible, we used this capability to reobserve fainter targets for which previous observations had not yielded a redshift. 20 – 50 sky fibers were distributed randomly in the 1° Hectospec field, avoiding known objects in SDSS, and at least ~ 5 of these were enforced to be in the central $3\frac{1}{2}$ radius.

3.1.1. Data reduction

We reduced Hectospec data using HSRED, a modification of the IDL SDSS pipeline written by R. Cool⁴ Papovich et al. (2006). HSRED computes a wavelength solution from HeNeAr arc lamp spectra, removes cosmic rays and flat-fields the 2-D images, extracts spectra using fiber traces determined from dome flat observations, and subtracts sky spectra averaged from sky fibers.

We determined the optimum number of sky fibers by comparing the noise induced by poor sky subtraction beyond 8000 \AA in object fibers for sets of up to 200 randomly-distributed sky fibers. Increasing the number of sky fibers beyond 50 resulted in no further discernible decrease in the noise. We improved sky subtraction over that provided in the HSRED pipeline by adjusting the amplitude and wavelength of the sky spectrum for each fiber to minimize residuals about the [OI] $\lambda 5577 \text{ \AA}$, Na 5893 \AA , and [OI] $\lambda 6300 \text{ \AA}$ sky lines.

We determined redshifts and object classifications for combined spectra with an automated code modified from the SDSS pipeline specBS for Hectospec. The pipeline finds the best linear combination of template spectra to

minimize χ^2 . The template spectra include 6 types of galaxy spectra and 4 types of QSOs. The galaxy templates range from early-type to late-type and include an LRG spectrum. To prevent sky-subtraction residuals from biasing the redshift solutions, we set the inverse variances at the locations of the thirty most prominent sky lines in the optical region ($3800 \text{ \AA} < \lambda < 8000 \text{ \AA}$) to zero.

We perform a visual inspection of all spectra and redshift solutions, assigning one of three classes: ‘A’ (clear redshift success), ‘B’ (possible redshift success), and ‘C’ (redshift failure). Only ‘A’ spectra are included in this paper, although the quantitative results do not change significantly if the ‘B’ spectra are included in the analysis. ‘A’ redshifts are assigned to 91% of the sample with reduced spectra. The positions, heliocentric redshifts, magnitudes, and estimated errors are tabulated in Table 3 for all objects with a secure, visually-confirmed assigned redshift.

3.1.2. Velocity zeropoint

The HSRED reduction package uses arc lamp spectra to determine the velocity zero point of the spectrograph on a nightly basis. However, telescope and instrument flexure between slews and observations potentially change the velocity zero point for individual configurations. We assess the magnitude of this effect by measuring the velocities of prominent night sky lines in individual spectra. For this procedure, we reduce each configuration without subtracting the sky as measured from sky fibers and ignore the Heliocentric correction. For all sky and object spectra in each configuration, we fit a single Gaussian to three prominent night sky lines (5577 \AA , 5890 \AA , 6300 \AA). The average zeropoint offset for all configurations is less than 10 km s $^{-1}$. The dispersion of the zeropoint offset for individual configurations varies from 4 to 7 km s $^{-1}$. Because these zeropoint offsets are significantly smaller than the quoted random errors, and could be due at least in part to errors in centroiding night sky lines, we do not correct for these offsets.

3.1.3. Internal errors

We assess internal redshift errors by comparing the redshifts measured for multiply-observed objects. To assess agreement at bright magnitudes, we use 14 bright galaxies ($19 < i_{AB} < 20.5$) observed twice in one hour configurations. For these objects, the mean redshift offset is 5.2 km s $^{-1}$ and the RMS dispersion is $\pm 34 \text{ km s}^{-1}$. We also use 42 re-observations of bright F stars ($15 < i_{AB} < 16$) to assess the internal error in very high S/N cases. For these stars, the mean velocity offset is $3.3 \pm 2.5 \text{ km s}^{-1}$ and the dispersion is $\pm 16 \text{ km s}^{-1}$. No catastrophic failures ($|\Delta z| > 0.01$ for galaxies or $|\Delta V| > 100 \text{ km s}^{-1}$ for

⁴ <http://www.astro.princeton.edu/~rcool/hsred/>

TABLE 2
SUMMARY OF DATA PARAMETERS FOR SUBARU ARCHIVAL IMAGING.

Beam name	Band	Date	Depth (3σ , AB) ^a	Exposure time (min)
0850	B	Dec 20, 2006	27.3	44
	V	Feb 23, 2004, Nov 29, 2005	27.3	52
	R_c	Dec 26, 2000, Mar 4-5, 2005	27.5	70
	I_c	Dec 26, 2000	26.7	56
	i'	Mar 5, 2005	26.6	30
	z'	Mar 5, 2005, Apr 26, 2003	26.2	62
1306	V	Mar 13-15, 2010	26.8	20
	i'	Mar 13-15, 2010	26.5	22

^aSensitivities are calculated from final stacked images using $1''.5$ diameter apertures.

TABLE 3
SPECTROSCOPIC DATA FOR GALAXIES IN EACH BEAM (COMPLETE
TABLE AVAILABLE IN ELECTRONIC VERSION)

RA (J2000)	Dec (J2000)	Redshift	i_{AB}
08 50 34.04	+36 00 55.5	0.1082 ± 0.00024	20.3
08 50 13.17	+36 01 45.1	0.3809 ± 0.00013	19.0
08 49 58.66	+36 03 57.7	0.3753 ± 0.00019	20.1
08 50 04.93	+36 04 11.8	0.3654 ± 0.00015	19.3
08 50 21.88	+36 03 23.3	0.6362 ± 0.00015	20.0
08 50 28.51	+36 03 16.7	0.2173 ± 0.00015	19.1

stars) are seen in either of these samples.

We also re-observed an entire “faint” configuration in poor seeing to estimate the redshift errors for galaxies with $20.5 < i_{AB} < 21.1$. Both observations received a 2 hour exposure time. The second observation yielded an average signal-to-noise that is 54% of the first observation due to poor seeing. Although this average S/N is lower than all other configurations and is unrepresentative of the overall sample, we assess the agreement between re-observations to place a conservative upper limit on the incidence rate of redshift failures. 100 objects were classified as galaxies (not QSOs or stars) with ‘A’ quality in the first configuration and 53 matching objects from this set were classified as galaxies with ‘A’ quality in the second observation. The reduced number of objects with ‘A’ quality in the second observation is due to the low S/N in that data. All of the matching redshifts agreed to within 0.001% ($\sim 300 \text{ km s}^{-1}$) with a maximum deviation of 252 km s^{-1} . For these matches, the mean velocity offset was $3.0 \pm 9.0 \text{ km s}^{-1}$ and the dispersion was $\pm 63 \text{ km s}^{-1}$. The deviations are Gaussian-distributed with extended tails. No matches with ‘A’ quality were catastrophic failures, including 10 additional matches classified as stars or QSOs. Because no catastrophic failures were seen for multiply-observed objects in bright configurations, the catastrophic failure rate is likely negligibly small ($< 1\%$). Since the second observation of the “faint” configuration had poor signal-to-noise not representative of the other Hectospec configurations, we believe that this upper limit on the failure rate is a conservative estimate.

3.1.4. Comparison to redshifts from external surveys

In general, we selected spectroscopic targets to avoid objects for which redshifts had been measured by other surveys. However, 24 galaxies from our overall Hectospec sample with $i < 19.6$ also have Sloan Digital Sky Survey

spectra (Aihara et al. 2011). The average difference between the Hectospec velocities and the SDSS velocities (both Heliocentric) is $-25.0 \pm 10 \text{ km s}^{-1}$, such that the average Hectospec redshift is blueshifted. The 1σ standard deviation about this value is 47.5 km s^{-1} . The distribution of deviations has no outliers, with minimum and maximum values of -101 and 60 km s^{-1} , respectively. The systematic offset of $-25.0 \pm 10 \text{ km s}^{-1}$ is less than the typical velocity error for objects with $18 < i < 21$ as measured with configuration re-observations, as described in the previous section, so we do not correct the zeropoint for this value.

3.1.5. Completeness

We plot the redshift success completeness, or the ratio of the number of ‘A’ quality spectra to the number of SDSS-identified galaxies, in Figure 1. We plot the completeness as a function of radius from the center of the field, galaxy color, and galaxy brightness. The completeness in beam 0850 is high, exceeding 80% for bright, central galaxies. Limited spectroscopic coverage beyond a radius of $r = 7.5'$ is available for beam 0850. Within a radius of $7.5'$, 0850’s completeness is generally flat as a function of field radius, target color, and target brightness. With completeness of 40% for bright central galaxies, beam 1306 is less complete than 0850. It lacks coverage beyond a radius of $7.5'$, but has some coverage at very faint magnitudes ($i' > 21.1$).

3.2. Archival Subaru Imaging

To search for lensed arcs in these beams, we make use of deep Subaru Suprime-Cam (Miyazaki et al. 2002) imaging in B , V , R_c , I_c , i' , and z' bands. These data were obtained from the Subaru-Mitaka-Okayama-Kiso Archive (SMOKA) archive (Baba et al. 2002). Images taken for 0850 were obtained as part of the MACS followup program and have been published previously (Hashimoto, Henry, & Böhringer 2008). Table 2 summarizes the imaging depths, exposure times, and bands.

Subaru Suprime-Cam images taken before January 2010 are reduced using the SDFRED1 package (Yagi et al. 2002; Ouchi et al. 2004) and those afterward with the SDFRED2 package (Yagi et al. 2002; Ouchi et al. 2004). We reduced images for 0850 with SDFRED1 and those for 1306 with SDFRED2. Both reduction pipelines subtract overscan and bias frames, combine flat field frames, correct the frames for distortion and atmospheric dispersion, subtract the sky background, mask the AG shade and bad pixels, and finally align, scale, and combine the

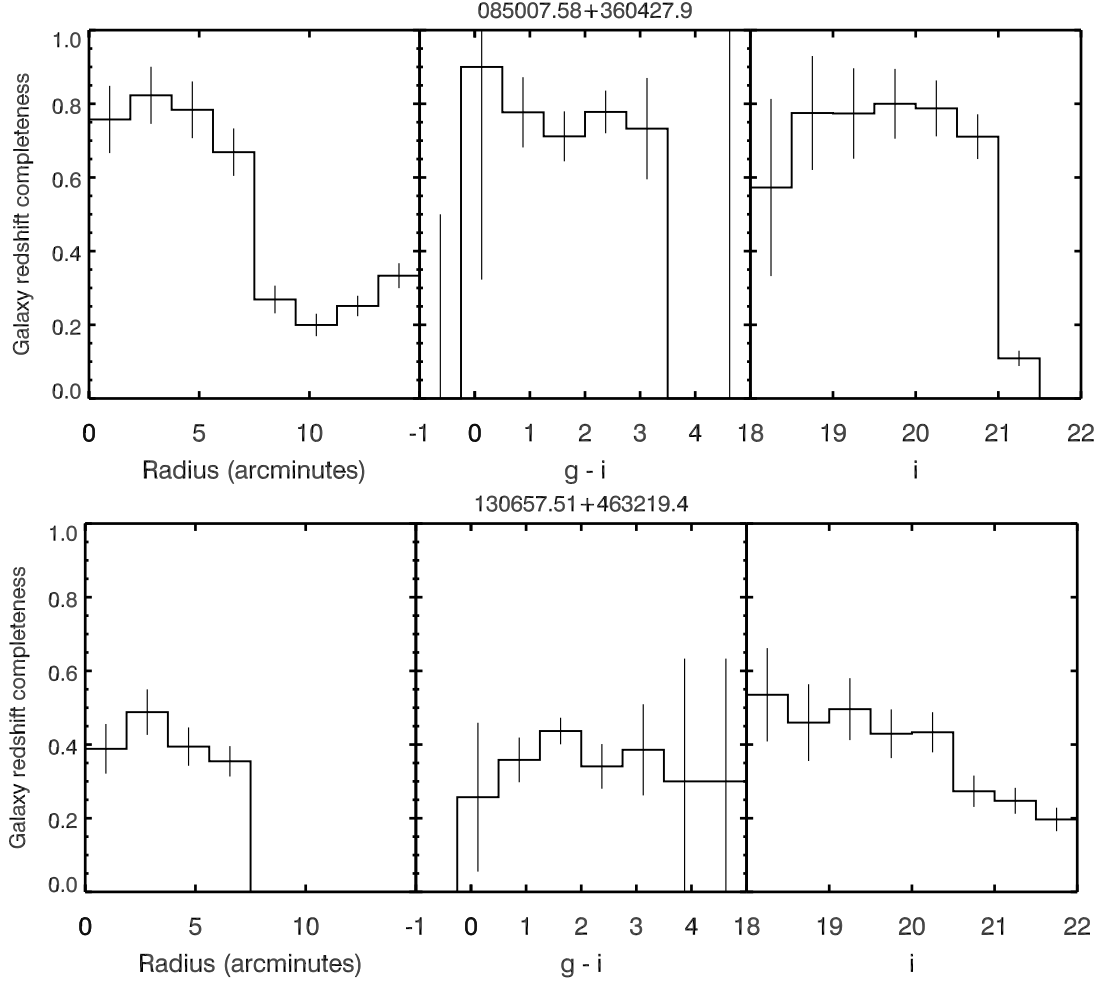


FIG. 1.— Redshift success completeness as a function of field radius, galaxy $g-i$ color, and galaxy i magnitude for 627 galaxies in beam 0850 and 332 galaxies in 1306. Error bars indicate the Poisson counting error for individual bins. The completeness is largely flat as a function of field radius, galaxy color, and magnitude, with the exception of the sparse sampling beyond $r = 7'$ in 0850 and $i_{AB} > 20.5$.

science frames. Flat frames were constructed from science frames in all bands for both 0850 and 1306.

Astrometric solutions and photometric zeropoints are determined for each band by matching Subaru star positions and photometry to sources detected in SDSS. We first run the SDFRED1 program *starselect.csh* on the Subaru bands, which calls Source Extractor (Bertin & Arnouts 1996) to measure source fluxes and dimensions. We select objects with peak fluxes less than 10,000 counts (unsaturated) lacking detected neighbors with more total flux than 2500 counts ($m \sim 24 - 25$) within $6''$ radius (isolated) and a Kron radius less than 2.4 pixels (stellar). The star positions are matched to SDSS coordinates with the program *match-0.14*, which uses the method of similar triangles (Valdes et al. 1995). We use a linear model matching shift, rotation, and plate scale. Subaru stellar photometry is measured with $6''$ diameter apertures with an aperture correction measured on more isolated stars (typically less than 0.03 magnitudes). SDSS PSF magnitudes in the $u'g'r'i'z'$ system are converted into UBVRI magnitudes with transformations on the SDSS DR5 website⁵ credited to R. Lupton, with quoted errors typically less than 1%.

Zeropoints, photometric agreement, and astrometric agreement are assessed for 50-300 stars in each band. Only objects classified as stellar by SDSS and satisfying the isolation and Kron radii criteria noted above are used for zeropoint calibrations. After setting photometric zeropoints, the average agreement between Subaru aperture photometry and SDSS PSF magnitudes over all bands is 0.065 magnitudes (1σ dispersion). To assess the photometric noise attributable to Subaru photometry alone, we subtract the known SDSS photometric errors for each star in quadrature from the measured dispersion for each band, and find an average 1σ dispersion of 0.056 magnitudes. The worst photometric agreement is seen in the R_C band, with 0.101 magnitudes of dispersion. The average dispersion in the astrometric positions with a linear model is 0.077 arcseconds.

4. RESULTS AND DISCUSSION

In this section, we describe the construction of group catalogs for each of the beams. Assessing halo membership and estimating velocity dispersions, virial radii, and virial masses reliably is essential to modeling the field magnification. Our approach for assessing galaxy membership and computing velocity dispersions follows techniques in Zabludoff, Huchra, & Geller (1990), Danese et al. (1980), Girardi et al. (1998), and Biviano et al. (2006). Virial masses are computed following Girardi et al. (1998) with the assumption that the virial theorem holds. The advantage of this approach is that masses can be estimated dynamically from galaxy redshifts and positions alone. The calculation can be performed for groups and sparsely-sampled clusters with as few as 10 members.

4.1. Constructing Group Catalogs

To identify structures in each beam, we first visually search for peaks in a redshift histogram that includes all secure, visually-confirmed redshifts in the field. Candidate halos are identified by selecting groups of more

than 10 objects clustered over a cosmologically corrected velocity range of at least 1500 km s^{-1} . Separate peaks adjacent in redshift are considered to be part of the same parent halo if they are separated by less than 1500 km s^{-1} .

For each candidate peak, galaxies are considered to be members of the halo if the velocity separation to the nearest member galaxy is less than 1500 km s^{-1} . Membership is assessing starting at the peak redshift and extending outward to both positive and negative relative velocity. For the resulting cluster members, we compute the mean cluster velocity v and projected velocity dispersion σ using the biweight estimators (Beers et al. 1990; Momcheva 2009). Interlopers are trimmed from halo membership by removing galaxies separated by more than 1σ from member galaxies.

4.2. Procedure for Estimating Virial Radii and Velocity Dispersions

Quantities such as velocity dispersion and virial radius R_{vir} are ideally estimated using galaxies within the virial radius. The dynamics of galaxies outside this radius may be affected by infall and are not appropriate for estimating halo properties. But the sensitive dependence of calculated virial radius on the aperture necessitates an iterative approach (Girardi et al. 1998). At the start of the iterations, we would like to apply an aperture a with constant physical dimensions to each halo to avoid biasing halo properties with redshift. This initial aperture must avoid extending beyond the field of view with spectroscopic coverage for all halo candidates.

We calculate this initial aperture by first computing the peak centroid of all candidate peaks. For each peak, we calculate the angular distance between the peak centroid and the edge of the field of view with spectroscopic coverage and convert this distance to physical units (Mpc). We then find the minimum distance to the edge of the field in physical units over all the halos and set the aperture radius a equal to this value. For 0850 and 1306, these distances are 2.42 Mpc and 1.46 Mpc, respectively. We perform the following steps for each candidate peak to arrive at self-consistent estimates of virial radius and velocity dispersion:

1. Within the aperture a , calculate mean velocity and velocity dispersion using the biweight estimators.
2. Restrict membership in redshift space with a conservative 3σ cut, assigning membership to galaxies satisfying (Zabludoff, Huchra, & Geller 1990; Yahil & Vidal 1997):

$$c\delta_z < 3\sigma_{in}(1+z)$$

3. Within the aperture a , recalculate peak centroid, mean velocity, and velocity dispersion with biweight estimators.
4. Estimate the virial radius with equation (9) of Girardi et al. (1998):

$$R_{vir} = 0.002\sigma$$

where σ is in units of km s^{-1} and R_{vir} is in units of Mpc. Set the aperture $a = R_{vir}$.

⁵ <http://www.sdss.org/dr5/algorithms/sdssUBVRITransform.html>

5. Restrict membership with a 3σ cut and recalculate peak centroid, mean velocity, and velocity dispersion within aperture a with biweight estimators.
6. Calculate the projected harmonic mean radius within the aperture a with equation (7) of Girardi et al. (1998):

$$R_{PV} = \frac{N(N-1)}{\sum_{i>j} R_{ij}^{-1}}$$

where R_{ij} is the distance between the i th and j th members and N is the number of halo members.

7. Estimate the virial radius with equation (9) of Girardi et al. (1998):

$$R_{vir}^3 = \frac{\sigma R_{PV}}{6\pi H_0^2}$$

and set the aperture $a = R_{vir}$.

We iterate steps 5-7 until the procedure has converged or the number of members is zero. We define convergence as the point at which the number of members and velocity dispersion estimate no longer changes from the previous iteration to the next. For all the halo candidates we identify in these two beams, the procedure converges or ends with zero members before 10 iterations is reached. Following the convergence, we estimate the virial mass of the halo with equation (5) from Girardi et al. (1998):

$$M_V = \frac{3\pi \sigma^2 R_{PV}}{2 G}$$

Note that this formula depends on the projected harmonic mean radius and not the virial radius.

4.3. Properties of Identified Groups

We treat groups that survive this iterative procedure with more than 10 members as virialized halos and include them in our mass model. The properties of these structures are tabulated in Table 4. Full redshifts histograms for both beams are shown in Figures 2 and 4. Redshift histograms and field maps are shown for each of the surviving groups in Figures 3 and 5.

The LRGs with spectroscopic redshifts within $r = 3/5$ of the center of 1306 appear to mark three structures, as shown in Figure 4; the mean redshifts of these LRGS are $z = 0.3782$, $z = 0.4754$, and $z = 0.5631$. The first of these corresponds to cluster 0850.1 identified in galaxy spectroscopy. The other two do not appear to be associated with structures as determined by our iterative procedure. There is no candidate peak in the field spectroscopy near $z = 0.4754$, suggesting that this LRG is either spurious or an isolated red galaxy in a small, sparsely sampled group. There is a candidate peak at $z = 0.563$ that converged on a $\sigma = 150 \pm 90 \text{ km s}^{-1}$ group with 4 members within the virial radius. Our field spectroscopy is not deep enough to recover this structure with substantial membership, but given its very small velocity dispersion estimate, it is unlikely that it would contribute significantly to the field magnification if real. Both of these candidate structures are flagged by individual LRGs.

The LRGs with spectroscopic redshifts within $r = 3/5$ of the center of 1306 appear to mark three structures, as

shown in Figure 4; the mean redshifts of these LRGS are $z = 0.2233$, $z = 0.3741$, and $z = 0.6019$. The redshifts of the three groups identified through field spectroscopy agree with these three structures, suggesting that they truly are virialized halos. The velocity dispersions of the two groups 1306.2 and 1306.3 are substantial, yet these groups are sparsely sampled with 10-18 members, so their association with LRGs is important in interpreting them as real.

As discussed in Section 2.2, previous studies have identified associations in these beams, including Zwicky 1953 in 0850 and Abell 1682 in 1306. Zwicky 1953 in 0850 at $z = 0.378$ (Zwicky et al. 1961) is very likely the same as the massive structure 0850.2 we identify at $z = 0.3774$. 0850 also has two photometrically identified associations at $z = 0.241$ and $z = 0.284$ (Hao et al. 2010). It is not immediately clear how these associations relate to the two groups we identify, although it is plausible that the $z = 0.284$ structure corresponds to Zwicky 1953 and the lower redshift object corresponds to the small group we found at $z = 0.2715$.

Abell 1682 in 1306 at $z = 0.2339$ (Abell 1989) corresponds to the massive structure 1306.1 we find at $z = 0.2265$. There are four other photometrically identified associations in the field of 1306, three of which are nearly the same redshift and likely correspond to Abell 1682: $z = 0.2081$ by Wen et al. (2009), $z = 0.245$ by Hao et al. (2010), and $z = 0.2508$ by Gal et al. (2003). The last photometric association at $z = 0.337$ (Hao et al. 2010) may correspond to the structure we identify at $z = 0.3746$.

4.4. Constraining Field Magnification

We build maps of field magnification from mass models using the multi-plane tool GRAVLENS (Keeton 2001) and methodology published in Wong et al. (2011). In this model, assigning NFW (Navarro, Frenk, & White 1997) halos to structures with velocity dispersions $\sigma > 300 \text{ km s}^{-1}$ and singular isothermal spheres to line-of-sight galaxies. NFW halos are assumed to be spherical, with concentrations determined from the results of simulations by Zhao et al. (2009). Halo masses for individual galaxies are drawn from the Faber-Jackson relation given their absolute magnitudes (Faber & Jackson 1976). The fraction of the total virial mass mass apportioned to group halo mass is fixed at 0.9. The resulting magnification maps for a source plane of $z = 2.5$ are shown in Figures 6 and 7.

We assess the errors in the magnification maps with a Monte Carlo simulation of the lensing fields, varying halo concentration, halo ellipticity, halo centroid, total mass, and the properties of individual galaxies over 1000 trials using GRAVLENS. A redshift 4.95 source plane is assumed for the simulation. The halo concentration and ellipticity are varied by amplitudes consistent with the observed scatter in the mass-concentration relation (Bullock et al. 2001). The halo centroid is varied according to a bootstrap resampling of the observed galaxy positions. The total mass, as constrained by the velocity dispersion, is also varied according to a bootstrap resampling of the galaxy positions and redshifts. The properties of individual galaxies are varied according to scatter in the Faber-Jackson relation (Bernardi et al. 2003) and the known photometric errors. The result of the Monte

TABLE 4
GROUP CANDIDATES IN BEAMS 0850 AND 1306.

ID	\bar{z}_{group}^a	# members	Centroid	Centroid Error ($''$)	σ_{los} (km s^{-1})	M_{200} ($\times 10^{14} M_{\odot}$)	R_v (Mpc)
0850_1	$0.2715^{+0.0004}_{-0.0004}$	14	08 50 17.1 +36 01 13	22	340^{+90}_{-70}	$0.9^{+0.4}_{-0.4}$	$0.9^{+0.1}_{-0.2}$
0850_2	$0.3774^{+0.0004}_{-0.0005}$	161	08 50 07.6 +36 04 35	12	1300^{+60}_{-60}	$33^{+3.1}_{-2.9}$	$3.2^{+0.1}_{-0.1}$
1306_1	$0.2265^{+0.0003}_{-0.0003}$	160	13 06 56.0 +46 31 37	14	1100^{+70}_{-60}	$19^{+2.2}_{-1.9}$	$2.6^{+0.1}_{-0.1}$
1306_2	$0.3746^{+0.0007}_{-0.0008}$	18	13 06 59.3 +46 33 44	29	750^{+150}_{-120}	$8.0^{+2.5}_{-2.7}$	$2.0^{+0.2}_{-0.3}$
1306_3	$0.6050^{+0.0011}_{-0.0011}$	10	13 07 10.3 +46 30 45	43	690^{+160}_{-130}	$6.6^{+2.6}_{-2.4}$	$1.9^{+0.2}_{-0.3}$

^aAll errors determined with bootstrap resampling.

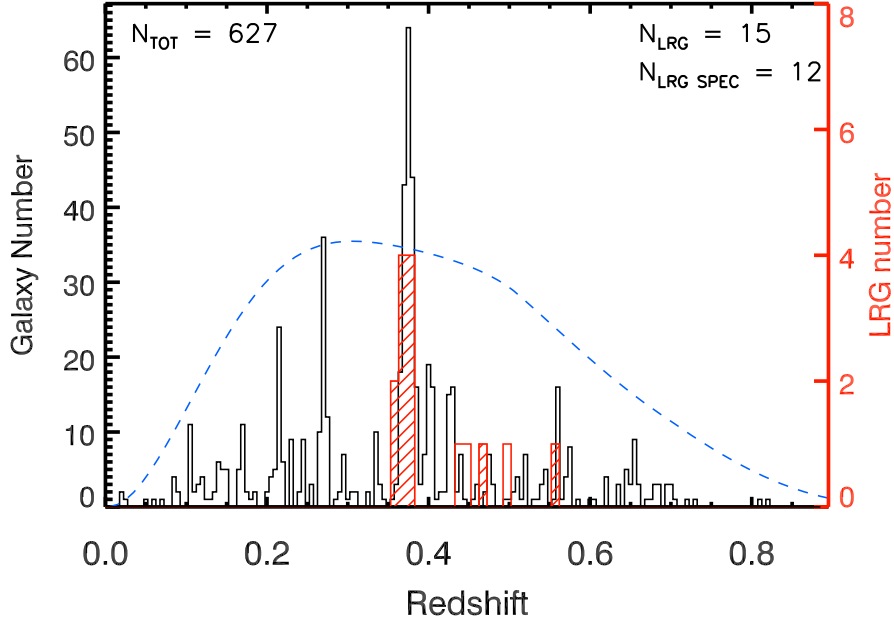


FIG. 2.— Spectroscopic redshift histogram for beam 0850 for 30 arcminute field diameter. The bin size is 1500 km s^{-1} . A redshift histogram for LRGs is overlaid in red, with photometric redshifts replaced by spectroscopic redshifts when available from SDSS or Hectospec. Spectroscopic redshifts for LRGs are denoted by a shaded histogram. The bin size for LRG histograms is 3000 km s^{-1} and the vertical units are marked on the rightmost y-axis. The blue dashed line is the redshift selection function for a homogeneous universe calculated using redshift completeness as a function of magnitude and field size with published luminosity functions for $0 < z < 1$ (Faber et al. 2007). The y-axis normalization for the redshift selection function is arbitrary. K-corrections are calculated from rest-frame M_B into observed i' using an LRG spectral template following Hogg et al. (2002). The histogram indicates the presence of multiple candidate structures in addition to a single dominant structure at $z \sim 0.375$.

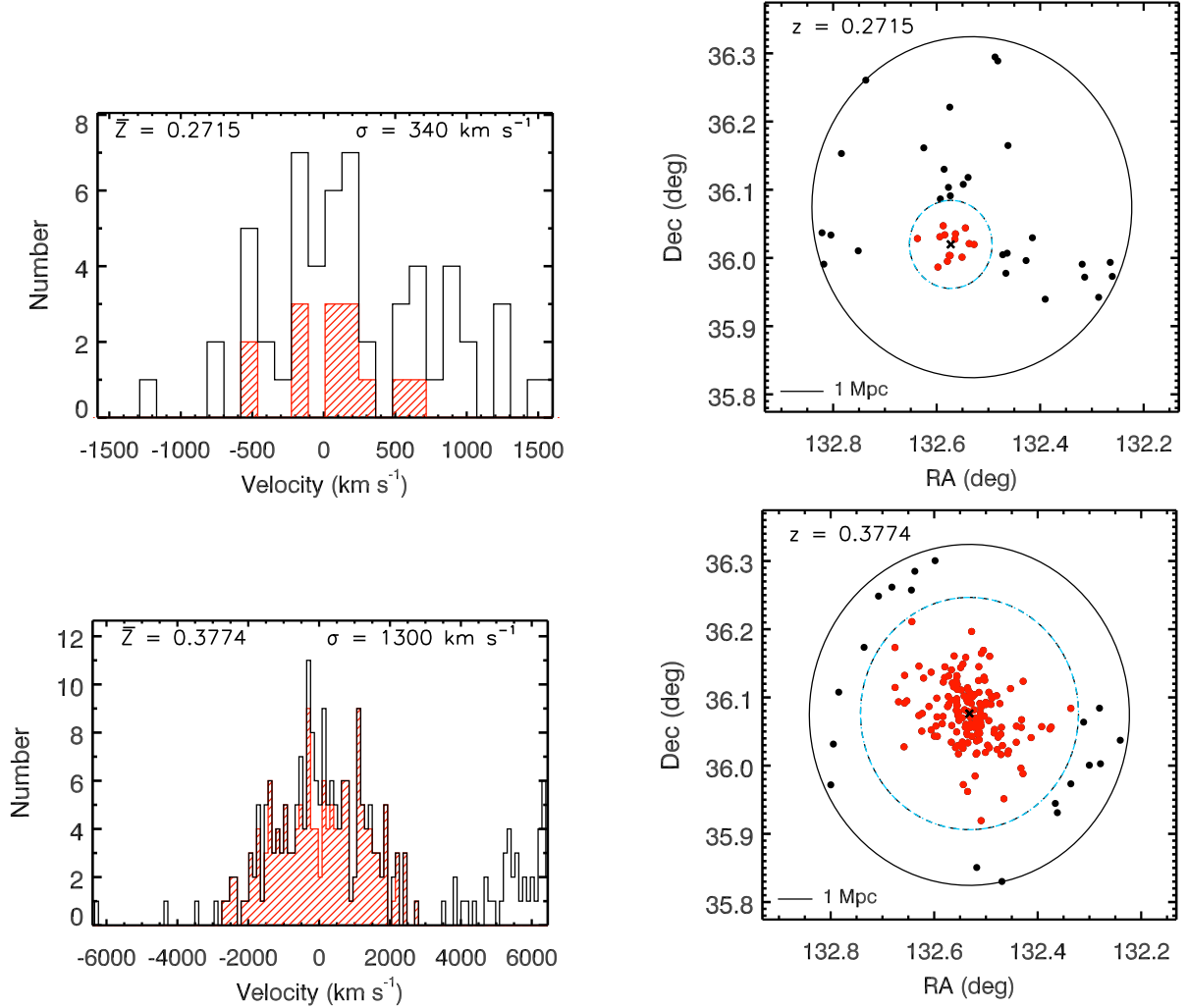


FIG. 3.— *Left*: Redshift histograms for two surviving peaks in beam 0850. The black histogram shows galaxies for a $30'$ arcminute field diameter and the red shaded histogram shows final members as determined by the iterative procedure described in Section 4.2. Bin size is 150 km s^{-1} . *Right*: Field maps showing members and nonmembers in each peak. The large black circle denotes the spectroscopic field, the black X marks the final peak centroid, and the blue dashed line shows the final calculated virial radius, which is used to select group members. The red filled circles denote group members (corresponding to red histogram in left panels). The black filled circles denote galaxies falling within 3σ of the peak velocity but are outside of the final calculated virial radius. Note that only a minority of galaxies within 3σ of the peak velocity in 0850.1 are classified as members, indicating substantial structure outside of a virial radius, although the velocity width of both the members and non-members is similar. In both peaks, the radius of virialization is completely circumscribed by the field selection circle, suggesting that group membership is not affected by a lack of redshifts beyond $r = 15'$.

Carlo is a distribution of 1000 magnification maps and traces of the tangential critical curve.

To compute the 1σ confidence contours of the tangential critical curve locations, we adopt a mean halo centroid over all the Monte Carlo trials. For each of 360 rays emanating from that point, evenly distributed in angle about 2π radians, we record the radii of the intersection points of the tangential critical curve with the ray for all Monte Carlo trials, including multiple intersections for individual trials if present. The 68% intervals in the distribution of radii for each ray define the positive and negative 1σ contours of the location of the critical curve for that angle. The results are shown in Figure 13 for beam 0850. The position of the inner contour is dominated by halo centroid uncertainty associated with averaging the positions of a finite sampling of galaxies.

4.5. Strongly-Lensed Arc Candidates in Subaru Imaging

We identify potential strongly-lensed arcs in both 0850 and 1306 in Figures 8 and 9 through visual inspection. Multiply-imaged arcs are particularly valuable for constraining the mass distribution in multiple-cluster systems, as they “pin down” the location of the critical curves for a source plane at a given redshift. We have identified a candidate multiply-imaged galaxy in beam 0850 in deep multi-band Subaru imaging of this field (see Figure 8) through the morphology and color information of the two components. The two adjacent components are both extended (with $L/W > 5$), are individually tangential to the radial vector pointing to the center of the nearby massive cluster, are both V-dropouts with $V - I > 2$, and have similar SEDs. The red V-R color in both components is highly suggestive of a Lyman break at $z \sim 5$, but could potentially be the 4000 Å/Balmer break in a lower-redshift, dusty galaxy. Their great distance from the center of the cluster ($55''$) suggests a large Einstein radius. Thus a validation of their photometric

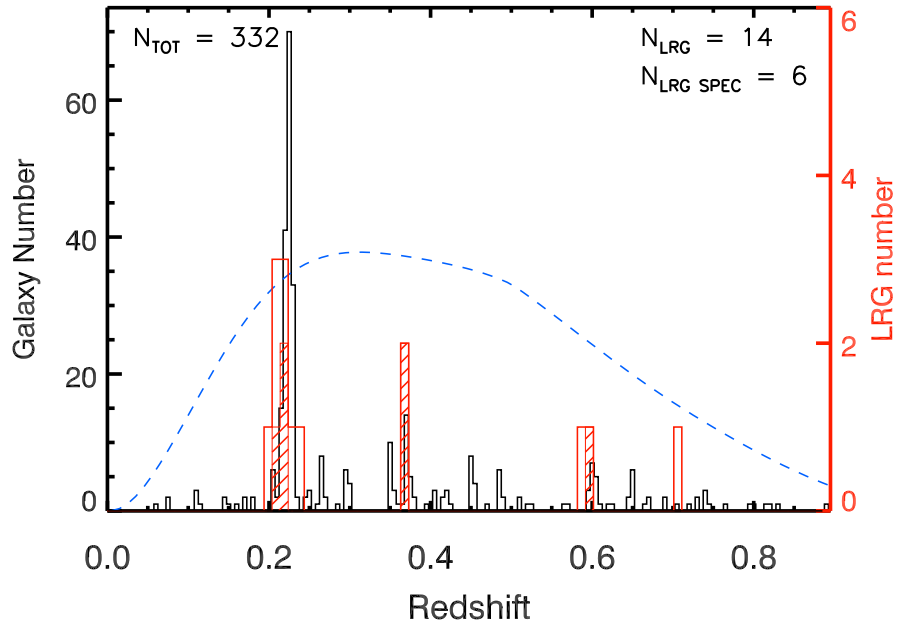


FIG. 4.— Redshift histogram for beam 1306 for 15' field diameter. Lines, symbols, and histograms follow Figure 2. In addition to a clear structure at $z \sim 0.22$, there are multiple candidate structures flagged by LRGs with spectroscopic redshifts (shaded histograms).

redshift estimate of $z \sim 5$ would confirm this beam as a massive cluster and corroborate the large velocity dispersion computed from the cluster galaxy redshifts.

To assess whether the dropout arcs 2 and 3 (Figures 8 and 10) are multiply-imaged, we compare the SEDs and photometric redshifts for both. Due to the potential contamination of arc photometry from lower-redshift galaxies, we use GALFIT (Peng et al. 2002) to remove adjacent galaxies before measuring photometry. We fit elliptical 2-D sersic profiles to three galaxies in the $15'' \times 15''$ region surrounding arcs 2 and 3. Residual images for each band are shown in Figure 11.

Photometry is measured on GALFIT residual images with elliptical apertures of axis ratio 2.8 and long axis $2''.8$, elongated in the direction of the extension of each arc. Sky background measurements are performed with annular elliptical apertures of axis ratio 2.8, inner radius $2''.8$, and outer radius $3''.5$. Photometric zeropoints are measured by comparing to SDSS photometry of unsaturated stars as described in Section 3.2. Error bars are determined for each band by performing aperture photometry with the same elliptical apertures on 50 non-overlapping blank regions in the $120'' \times 120''$ region surrounding the center of the beam, computing the 68% confidence intervals on the resulting flux distribution, and combining the result with the known zeropoint error for each band. The positive 68% confidence interval is quoted as the 1σ upper limit for non-detections. These upper limits match the values computed with the online Subaru Suprime-Cam Exposure Time Calculator to within 0.3 magnitudes in all bands for photometric apertures of comparable area, assuming point sources and $0''.7$ seeing.

Aperture photometry for 0850 arc candidates 2 and 3 is plotted in the top panel of Figure 12. Excluding non-detections in the *B* and *V*-bands, the photometry of the two arcs matches to within 1σ in all bands, suggesting that the two sources are multiple images of the same galaxy.

To be bona-fide multiply-imaged arcs, sources 2 and 3 would need to be located near the critical curve; but their significant distance of $55''$ away from the central BCG suggests that they must also be at high redshift ($z > 2$). Here, we use the public photometric redshift code BPZ (Benitez et al. 2000) to estimate photometric redshifts for the two arcs independently. This template-fitting code uses a Bayesian approach with priors of redshift probability as a function of galaxy type and magnitude. For this analysis, we retain the priors that are shipped with BPZ, which had been generated for objects with spectroscopic redshifts in the Hubble Deep Field and were judged to be superior to a flat redshift prior (Benitez et al. 2000). This is a rather conservative choice, as such priors reduce the probability of finding high-redshift solutions for bright sources, including sources made apparently bright by high magnification. The i' filter is used as a separate constraint with the I_c filter.

The bottom panel of Figure 12 plots the resulting redshift probability distributions for both arcs. The most likely redshift is found to be $z = 4.95$ for arc 2 and $z = 4.96$ for arc 3. The 1σ confidence intervals are $4.71 < z < 5.09$ for arc 2 and $4.73 < z < 5.05$ for arc 3. The probabilities of the high redshift solution being correct are 96.9% for arc 2 and 99.3% for arc 3. The best

fit template SED for arc 2 is plotted in the top panel of Figure 12. For comparison, an SSP model judged to be the best fit low-redshift solution to the data for arc 2 is plotted as a dashed green line. Although both models appear to match adequately for bands redder than *V*, the majority of the discriminating power comes from non-detections in *B* and *V*.

The predicted critical curve for a source redshift of $z = 4.95$ is shown in Figure 13. The critical curve is predicted from a mass model constrained by redshifts of field galaxies alone. Notice that there is broad agreement between the location of the critical curve and the positions of the two arcs, suggesting that they are located at high magnification.

The similar photometric redshifts of arcs 2 and 3 lends further evidence to the interpretation that they are multiple images of a $z \sim 5$ galaxy. The reader is cautioned that the extreme closeness of the most likely values ($z = 4.95$ and 4.96) is a product of the particular shapes of the red SEDs and should not be taken as freestanding hard evidence of a relation between the two arcs, given the considerable confidence intervals of $\sigma_z/z = 3.8\%$ for arc 2 and $\sigma_z/z = 3.2\%$ for arc 3. However, a number of lines of evidence suggest that they are multiply-imaged, including the similarity of the photometric redshifts, SEDs, and morphologies, and their alignment with the predicted tangential critical curve in both distance from the cluster center and position angle of extension.

5. CONCLUSIONS

Other clusters with large étendue have been discovered, and the two beams we present here are comparable or superior to these in many observables. For example, MACS0717+3745 has a considerable region of high magnification (3.2 square arcminutes with $\mu > 10$) generated by a shallow, unrelaxed inner mass profile (Zitrin et al. 2009, 2011).

MACS 1206-0847 is a member of MACS sample and is the most massive cluster in CLASH sample with an estimated virial mass of 3.7×10^{15} solar masses (Postman et al. 2012). As seen in Figure 6, the predicted critical curves for beam 0850 at a source plane of $z = 1$ are larger than those traced by $z \sim 1$ arcs seen in WFC3 imaging of MACS 1206-0847, suggesting a larger region of high magnification in 0850. The large radius of the critical curves is confirmed by the positions of morphologically-identified strongly-lensed arcs (Figure 10).

In this study, we have presented 979 MMT Hectospec redshifts in the fields of two lines of sight selected from the SDSS for their high integrated LRG luminosity densities, 0850 and 1306. We assembled group catalogs from the spectroscopy and identified five groups and cluster-scale halos in these two beams. The four of five of these structures surpassing group-scale ($\sigma > 500$ km s^{-1}) are also flagged by LRGs that have spectroscopic redshifts available. We estimated the virial radii and virial masses for these halos following established techniques in Zabludoff, Huchra, & Geller (1990) and Girardi et al. (1998). The integrated virial masses of these beams are substantial, with $3.4^{+0.3}_{-0.3} \times 10^{15} M_\odot$ for 0850 and $3.4^{+0.4}_{-0.4} \times 10^{15} M_\odot$ for 1306. We constructed mass models for these beams with inputs from the group catalogs only and computed magnification maps. The magni-

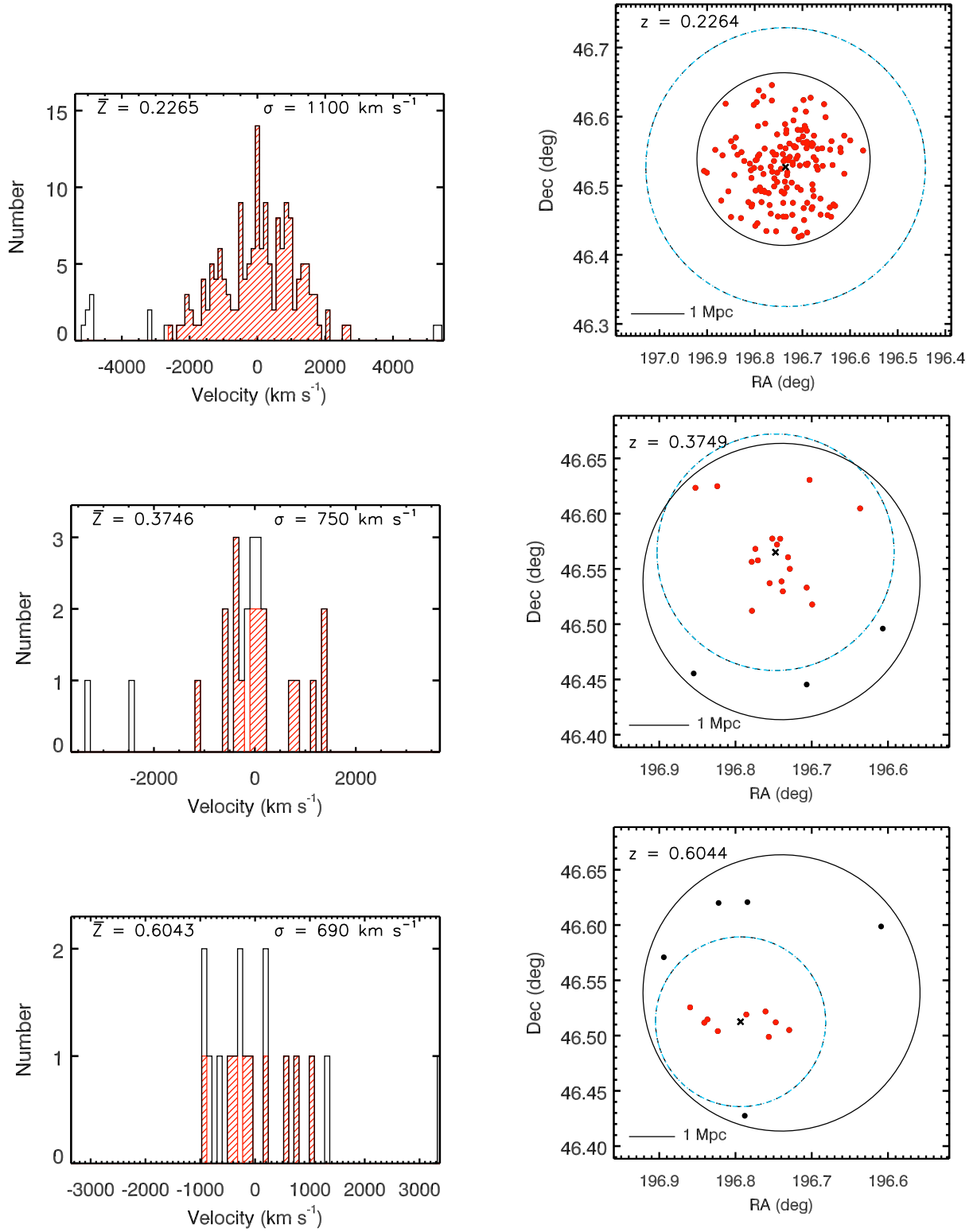


FIG. 5.— Redshift histograms and field maps for three peaks in beam 1306 for 15 arcminute field diameter. Lines, histograms, and symbols follow Figure 3. Note that the radius of virialization is substantially larger than the field selection circle of $r = 7.5$ for the cluster 1306.1 (Abell 1682), suggesting that incompleteness may bias the estimate of the velocity dispersion. The other two peaks 1306.2 and 1306.3 have membership circles that are circumscribable by the field radius, or nearly so, indicating that estimates of group properties are not affected by incompleteness outside of $r = 7.5$ for these peaks.

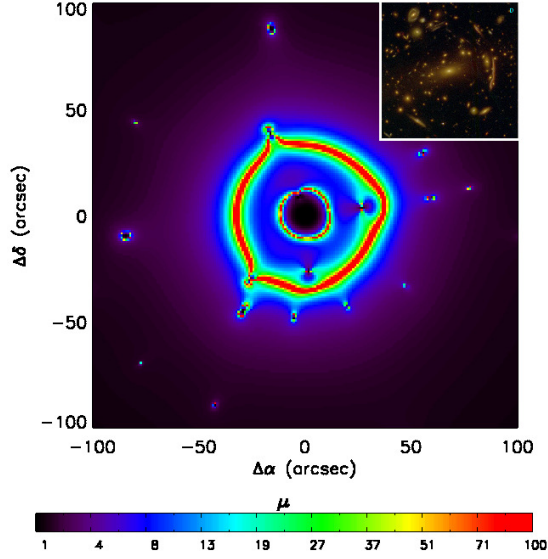


FIG. 6.— Magnification map for beam 0850 for a $z = 1$ source plane in a $200'' \times 200''$ field of view. An ACS/WFC3 image of MACS1206-0847 is included in the upper right for comparison at the same spatial scale (Postman et al. 2012).

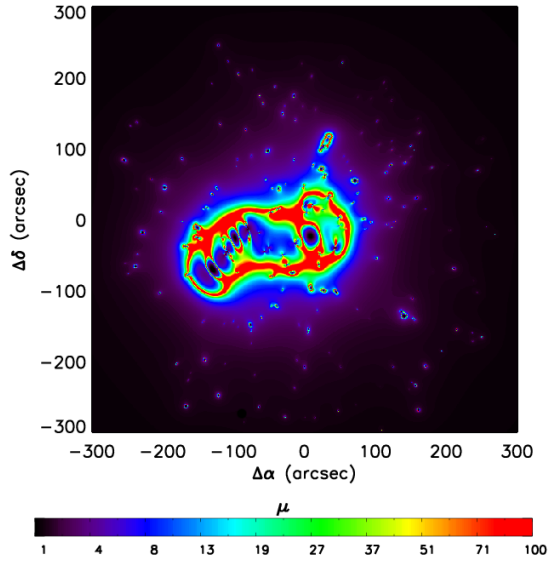


FIG. 7.— Magnification map for beam 1306 for a $z = 1$ source plane in a $600'' \times 600''$ field of view.

mification maps suggest substantial fields of high magnification. We also present a new serendipitous multiply-imaged source at $z = 4.95$ in 0850 seen in archival deep Subaru SuprimeCam imaging. Both components of the multiply-imaged source are V-dropouts, with a significant probability ($> 97\%$) of being at $z = 4.95$. The multiple-imaging interpretation of these sources is strengthened by the similarity of the photometric redshifts, SEDs, and morphologies, and their alignment tangential to a vector pointing toward the most massive cluster in the beam. The critical curve position in 0850 for a source plane of $z = 4.95$ is consistent with the location of the multiply-imaged candidate, confirming the prelim-

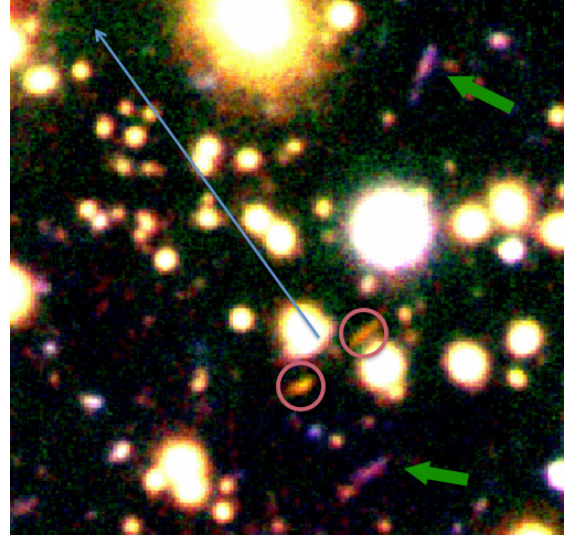


FIG. 8.— Subaru/SuprimeCam image ($1'0 \times 1'0$) containing the candidate multiply-imaged galaxy in beam 0850, with components denoted by magenta circles. Green arrows mark other candidate arcs in the field. The blue vector points to the center of the cluster.

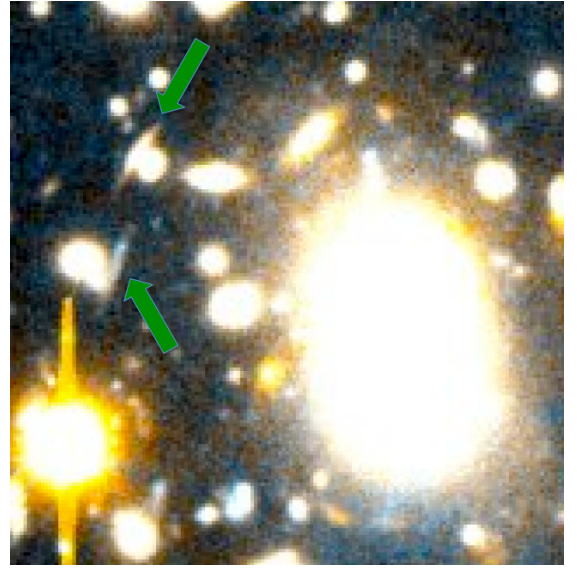


FIG. 9.— New candidate strongly-lensed arcs in beam 1306. Sand et al. (2005) presents two arc candidates seen in WFPC2 imaging (not shown).

inary mass model and the lensing power of the beam.

ACKNOWLEDGEMENTS

Thanks to Chang You and Decker French for assistance in gathering MMT Hectospec data. Thanks also to Dan Marrone, Brant Robertson, Sandy Faber, Pascal Oesch, Greg Walth, Michael Schneider, and Kristian Finlator for productive conversations. Support for Program number HST-HF-51250.01-A was provided by NASA through a Hubble Fellowship grant from the Space Telescope Science Institute, which is operated by the Association of Universities for Research in Astronomy, Incorporated, under NASA contract NAS5-26555. AIZ and KCW acknowledge support from NASA through programs NNX10AD47G and NNX10AE88G and NSF sup-

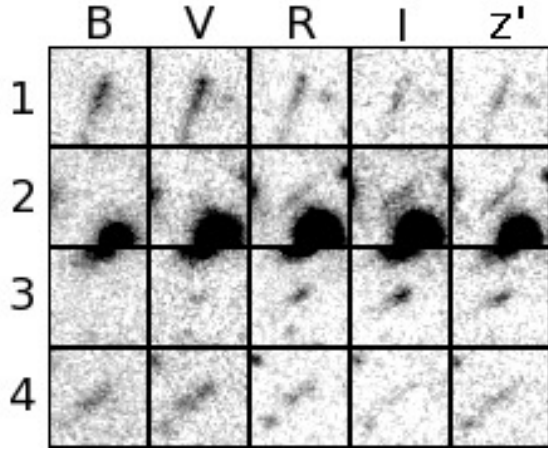


FIG. 10.— Subaru Suprime-Cam images of four candidate strongly-lensed arcs in beam $0850, 8''.0 \times 8''.0$. The z band is used for the red channel, $R + I + i$ for the green channel, and $B + V$ for the blue channel. Each row denotes images of a different arc and columns show images in a different band, as labeled. Notice that arcs 2 and 3 are less visible in the B and V bands.

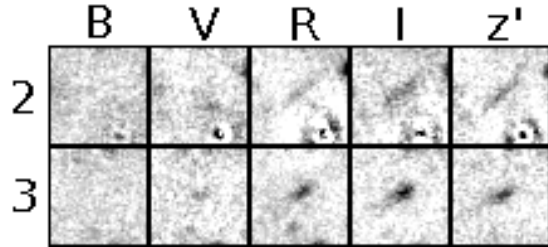


FIG. 11.— Subaru Suprime-Cam images of two candidate multiply-imaged arcs in beam $0850, 8''.0 \times 8''.0$. Nearby galaxies have been subtracted with GALFIT. Each row denotes images of a different arc and columns show images in a different band, as labeled.

port through AAG program 1211874. This work is based in part on data collected at Subaru Telescope and obtained from the SMOKA, which is operated by the Astronomy Data Center, National Astronomical Observatory of Japan. Observations reported here were obtained at the MMT Observatory, a joint facility of the University of Arizona and the Smithsonian Institution. This research has made use of the SIMBAD database, operated at CDS, Strasbourg, France. This paper uses data products produced by the OIR Telescope Data Center, supported by the Smithsonian Astrophysical Observatory. This work performed under the auspices of the U.S. Department of Energy by Lawrence Livermore National Laboratory under Contract DE-AC52-07NA27344 with document release number XXX.

REFERENCES

- Abell, G.O., et al. 1989, *ApJS*, 70, 1
Ahn, C.P., et al. 2012, *ApJS*, 203, 21
Aihara, H., et al. 2011, *ApJS*, 195, 26
Baba, H., et al. 2002, *ADASS XI*, eds. D. A. Bohlender, D. Durand, & T. H. Handley, ASP Conference Series, 281, 298
Bahcall, J. & Tremaine, S. *ApJ*, 244, 805
Barrena, R., Boschin, W., Girardi, M., & Spolaor, M. 2007, *A*, 469, 861
Beers, T., Flynn, K., & Gebhardt, K. 1990, *AJ*, 100, 32
Böhringer, H., Voges, W., Huchra, J., et al. 2000, *ApJS*, 129, 435
Benitez, N. 2000, *ApJ*, 536, 571
Bernardi, M., et al. 2003, *AJ*, 125, 1849
Bertin, E. & Arnouts, S. 1996, *ApJS*, 317, 393
Biviano, A., Katgert, P., Thomas, T., & Adami, C. 2002, *A*, 387, 8
Biviano, A., Murante, G., Borgani, S., Diaferio, A., Dolag, K., & Girardi, M. 2006, *A*, 456, 23
Bouwens, R., et al. 2008, *ApJ*, 686, 230
Bouwens, R., et al. 2009, *ApJ*, 690, 1764
Bouwens, R., Illingworth, G., González, V., et al. 2010, *ApJ*, 725, 1587
Bouwens, R., et al. 2011, *Nature*, 469, 504
Bouwens, R., et al. 2012, *arXiv:1211.2230*
Bradač, M., et al. 2009, *ApJ*, 706, 1201
Bradač, M., et al. 2012, *ApJ*, 755, 7
Bradley, L., et al. 2008, *ApJ*, 678, 647
Broadhurst, T., Taylor, A., & Peacock, J. 1995, *ApJ*, 438, 49
Broadhurst, T. & Lehar, J. 1995, *ApJ*, 450, 41
Bullock, J., et al. 2001, *MNRAS*, 321, 559
Bunker, A., et al. 2010, *MNRAS*, 409, 855
Cavagnolo, K., Donahue, M., Voit, G.M., & Sun, M. 2009, *ApJS*, 182, 12
Coe, D., et al. 2013, *ApJ*, 762, 32
Crawford, C.S., Allen, S.W., Ebeling, H., et al. 1999, *MNRAS*, 306, 857
Danese, L., de Zotti, G., & di Tullio, G. 1980, *A&A*, 82, 322
Diaferio, A., et al. 1999, *MNRAS*, 309, 610
Djorgovski, S. G., Odewahn, S. C., Gal, R. R., et al. 1999, *BAAS*, 194, 04.14
Dressler, A. & Shectman, S. 1988, *ApJ*, 95, 985
Ebbels, T., et al. 1996, *MNRAS*, 281, 75
Ebeling, H., Edge, A., Böhringer, H., et al. 1998, *MNRAS*, 301, 881
Ebeling H., Edge A.C., & Henry J.P. 2001, *ApJ*, 553, 668
Ellis, R., et al. 2012, *arXiv:1211.6804v1*
Faber, S.M. & Jackson, R.E. 1976, *ApJ*, 204, 668
Faber, S.M., et al. 2007, *ApJ*, 665, 265
Fabricant, D., Fata, R., Roll, J., et al. 2005, *PASP*, 117, 1411
Kneib, J.-P., Ellis, R., Santos, M., & Richard, J. 2004, *ApJ*, 607, 697
Franx, M., et al. 1997, *ApJ*, 486, 75
Frye, B. & Broadhurst, T. 1998, *ApJ*, 499, 115
Gal, R.R., de Carvalho, R.R., Lopes, P., et al. 2003, *AJ*, 125, 2064
Girardi, M., Giuricin, G., Mardirossian, F., Mezzetti, M., & Boschin, W. *ApJ*, 505, 74.
Gladders, M. & Yee, H. 2000, *AJ*, 120, 2148
Hall, N., Bradač, M., Gonzalez, A., et al. 2012, *ApJ*, 745, 155
Hao, J., McKay, T., Koester, B., et al. 2010, *ApJS*, 191, 254

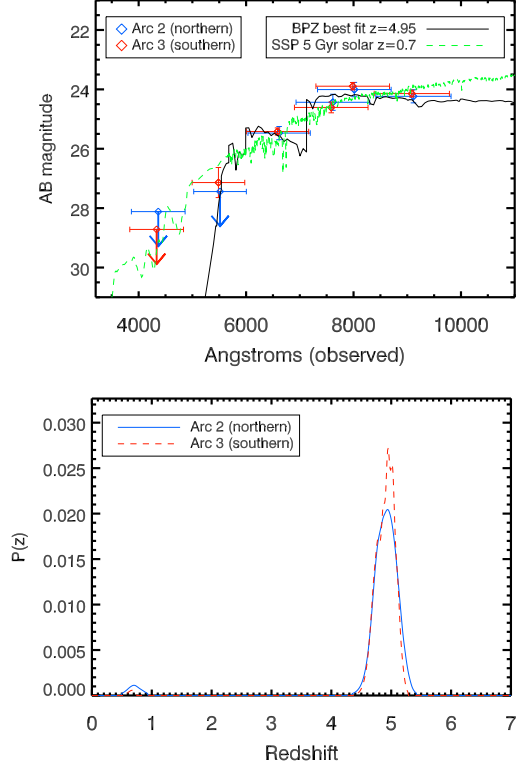


FIG. 12.— Top: SEDs for two multiply-imaged V-dropout objects in beam 0850 as a function of observed wavelength. Blue diamonds mark the photometric points of arc 2 (northern) and red diamonds mark those of arc 3 (southern). The photometry for arc 3 is shifted fainter by 0.6 magnitudes for display purposes. The B-band photometric measurements and the V-band measurement for arc 2 are 1-sigma upper limits. The solid black line is the best-fit single stellar population (SSP) model at redshift $z = 4.95$, identifying the break at $\sim 6000 \text{ \AA}$ as the Lyman Break. The best-fit low-redshift template solution for $z = 0.7$ is shown as a dashed green line. The majority of the discriminating power is provided by the *B* and *V*-band constraints. Bottom: BPZ photometric redshift probability distributions for both lensed arcs.

Hashimoto, Y., Henry, P., & Boehringer, H. 2008, MNRAS, 390, 1562
Hogg, D.W., Baldry, I.K., Blanton, M.R., & Eisenstein, D.J. 2002, arXiv:astro-ph/0210394
Keeton, C. 2001, preprint (arXiv:astro-ph/0102340)
Lemze, D., et al. 2009, ApJ, 701, 1336
Miyazaki, S., et al. 2002, PASJ, 54, 833
Mink, D., Wyatt, W., Caldwell, N., et al. 2007, ASPC, 376, 249
Momcheva, I. 2009, PhD dissertation, University of Arizona. Ann Arbor: ProQuest/UMI. (Publication No. AAT 3350066)
Navarro, J., Frenk, C., & White, S. 1997, ApJ, 490, 493
Oesch, P., Bouwens, R., Carollo, C., et al. 2010, ApJ, 709, 21
Oesch, P., et al. 2012, ApJ, 745, 110
Ouchi, M., et al. 2004, ApJ, 611, 660
Padmanabhan, N., Schlegel, D., Seljak, U., et al. 2007, MNRAS, 378, 852

Papovich, C., et al. 2006, AJ, 132, 231
Peng, C.Y., Ho, L.C., Impey, C.D., & Rix, H.-W. 2002, AJ, 214, 266
Postman, M., et al. 2012, ApJS, 199, 25
Richard, J., et al. 2006, A, 456, 861
Richard, J., et al. 2008, ApJ, 685, 705
Sand, D., et al. 2005, 627, 32
Stark, D., et al. 2007, ApJ, 663, 10
Wen, Z.L., Han, J.L., & Liu, F.S. 2009, ApJS, 183, 197
Wilman, D., Balogh, M., Bower, R., et al. 2005, MNRAS, 358, 71
Wong, K.C., Keeton, C., et al. 2011, ApJ, 726, 84
Wong, K.C., Ammons, S.M., Keeton, C., & Zabludoff, A. 2012, ApJ, 752, 104

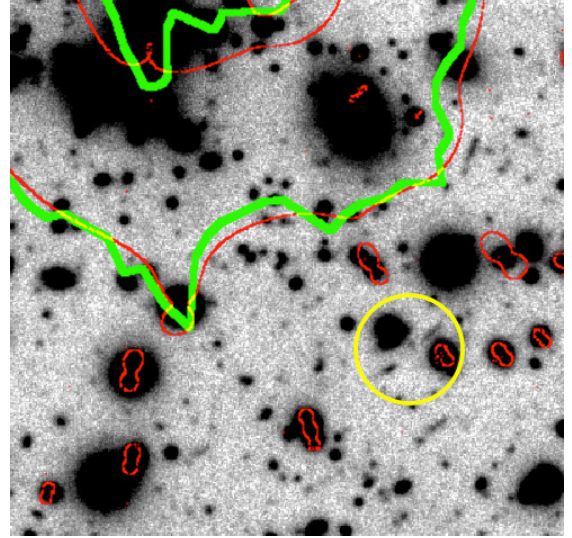


FIG. 13.— Expanded view of the multiply-imaged candidate in beam 0850 (1.5×1.5). Both components (magenta circles) are V-dropouts with a maximum-likelihood photometric redshift of $z = 4.95$. Predicted critical curves for a $z = 4.95$ source plane are shown in red. The location and orientation of the critical curves for this source plane, as determined by our mass model derived from Hectospec spectroscopy alone, are roughly consistent with the candidate's location.

Wong, K.C., Zabludoff, A., Ammons, S.M., Keeton, C., et al. 2013, submitted to ApJ
Valdes, F., et al. 1995, PASP, 107, 1119
Yagi, M., et al. 2002, AJ, 123, 66
Yahil, A., & Vidal, N.V. 1977, ApJ, 214, 347
Yan, H.-J., et al. 2010, Research in Astronomy and Astrophysics, 10, 867
Zabludoff, A., Huchra, J., & Geller, M. 1990, ApJ, 74, 1
Zhao, D., Jing, Y., Mo, H., & Börner, G. 2009, ApJ, 707, 354
Zheng, W., et al. 2009, ApJ, 697, 1907
Zheng, W., et al. 2009, Nature, 489, 406
Zitrin, A., Broadhurst, T., Rephaeli, Y., et al. 2009, ApJ, 707, 102
Zitrin, A., Broadhurst, T., Barkana, R., et al. 2011, MNRAS, 410, 1939
Zwicky, F. 1937, Phys. Rev. Lett., 51, 290
Zwicky, F., Herzog, E., Wild, P., Karpowicz, F., & Kowal, C.T. 1961, Catalogue of galaxies and clusters of galaxies, Vol I